Nano Research 2018, 11(3): 1687–1698
https://doi.org/10.1007/s12274-017-1786-x
Research Article
ISSN 1998-0124
CN 11-5974/O4

High-metallic-phase-concentration $Mo_{1-x}W_xS_2$ nanosheets with expanded interlayers as efficient electrocatalysts

Qun He[1,§], Yangyang Wan[2,§], Hongliang Jiang[1,§], Chuanqiang Wu[1], Zhongti Sun[2], Shuangming Chen[1] (✉), Yu Zhou[1], Haiping Chen[1], Daobin Liu[1], Yasir A. Haleem[1], Binghui Ge[3], Xiaojun Wu[2] (✉), and Li Song[1] (✉)

[1] *National Synchrotron Radiation Laboratory, CAS Center for Excellence in Nanoscience, University of Science and Technology of China, Hefei 230029, China*
[2] *CAS Key Lab of Materials for Energy Conversion, CAS Center for Excellence in Nanoscience, Hefei National Laboratory for Physical Science at the Microscale, Synergetic Innovation of Quantum Information & Quantum Technology, University of Science and Technology of China, Hefei 230026, China*
[3] *Beijing National Laboratory for Condensed Matter Physics, Institute of Physics, Chinese Academy of Sciences, Beijing 100190, China*
[§] *Qun He, Yangyang Wan and Hongliang Jiang contributed equally to this work.*

Received: 4 May 2017
Revised: 25 July 2017
Accepted: 31 July 2017

KEYWORDS

wet-chemistry, gram-scale synthesis, interlayer intercalation, metallic transition metal dichalcogenide, electrocatalytic water splitting

ABSTRACT

In most cases, layered transition metal dichalcogenides (LTMDs), containing metallic phases, show electrochemical behavior different from their semiconductor counterparts. Typically, two-dimensional layered metallic 1T-MoS_2 demonstrates better electrocatalytic performance for water splitting compared to its 2H counterpart. However, the characteristics of low metallic phase concentration and poor stability limit its applications in some cases. Herein, we demonstrate a simple and efficient bottom-up wet-chemistry strategy for the large-scale synthesis of nanoscopic ultrathin $Mo_{1-x}W_xS_2$ nanosheets with enlarged interlayer spacing and high metallic phase concentration. Our characterizations, including X-ray absorption fine structure spectroscopy (XAFS), high-angle annular dark-field-scanning transmission electron microscopy (HAADF-STEM), and X-ray photoelectron spectroscopy (XPS) revealed that the metallic ultrathin ternary $Mo_{1-x}W_xS_2$ nanosheets exhibited distorted metal–metal bonds and a tunable metallic phase concentration. As a proof of concept, this optimized catalyst, with the highest metallic phase concentration (greater than 90%), achieved a low overpotential of about –155 mV at a current density of –10 mA/cm^2, a small Tafel slope of 67 mV/dec, and an increased turnover frequency (TOF) of 1.3 H_2 per second at an overpotential of –300 mV (vs. reversible hydrogen electrode (RHE)), highlighting the importance of the metallic phase. More importantly, this study can lead to a facile solvothermal route to prepare stable and high-metallic-phase-concentration transition-metal-based two-dimensional materials for future applications.

Address correspondence to Li Song, song2012@ustc.edu.cn; Shuangming Chen, csmp@ustc.edu.cn; Xiaojun Wu, xjwu@ustc.edu.cn

1 Introduction

Large-scale hydrogen production through water splitting plays a vital role in the field of clean and renewable energy [1–5]. Platinum and some other noble metals are the most effective electrocatalysts for the electrochemical hydrogen evolution reaction (HER), and can achieve very low overpotential and electrochemical stability [6]. However, their widespread utilization is severely limited by their high cost and relatively low reserves [7–10]. Therefore, the development of nonprecious and efficient alternative HER electrocatalysts is urgent. To date, many researchers have focused their attention on finding new inexpensive electrocatalysts that can decrease the HER overpotential [11]. In the past, a wide range of alternatives like transition metal oxides, nanocarbon materials, etc., have been intensively explored [12–16]. In recent years, theoretical and experimental work have revealed that layered MX_2 (M = transition metal, X = S, Se, etc.) materials are promising electrocatalysts for HER due to the existence of electrocatalytically active sites at their metallic edges [17]. Thus, increasing the density of exposed metallic sites has been one of the main strategies to improve their electrochemical performance [18]. The formation of few-layered compounds has proved to be a feasible way to improve metallic characteristics and enhance HER performance. Few-layered transition metal dichalcogenides (LTMDs), such as MoS_2, WS_2, $MoSe_2$, and WSe_2, have proved to be better HER electrocatalysts because of their unique chemical and electronic features [19–26]. Other researchers have revealed that TMDs with ternary compositions, such as $MoS_{2(1-x)}Se_{2x}$, $Mo_xW_{(1-x)}S_2$, $WS_{2(1-x)}Se_{2x}$, $MoS_{2(1-x)}P_x$, and MoS_xCl_y, can further improve HER performance due to the increase in the concentration of exposed active sites [18, 27–31]. However, the concentration of active edge sites in 2H-MX_2 is always limited, thus restricting its HER kinetics. Therefore, the practical use of LTMD materials as alternatives to Pt remains a challenge [25, 32–34].

The structure and reactivity of MX_2-type LTMDs have been extensively explored for several decades [35]. Recently, some researchers found that 1T-MoS_2 and 1T-WS_2, which have distorted layer units in contrast with their 2H phases, can achieve superior HER performance, because the metallic 1T phase existing on the surface can improve their intrinsic catalytic nature [17, 36–38]. In addition to their exposed active sites, their higher electrical conductivity compared to their semiconducting counterparts would further enhance the electrochemical behavior [39]. We have recently developed a bottom-up wet-chemistry method to synthesize metallic MX_2 materials, such as WS_2 and MoS_2, on a gram-scale [40, 41]. The obtained materials were demonstrated to be useful in various fields, such as catalysis and photothermal therapy [41, 42]. Given the positive effect of many-component systems, we propose that ternary LTMDs with metallic phases should exhibit enhanced catalytic activity compared to binary mixtures of their components. In fact, ternary metallic TMDs have previously been reported, but the obtained materials had very low metallic phase concentrations and low yields [43]. Therefore, to the best of our knowledge, no gram-scale synthesis for ternary LTMDs with high metallic phase concentration has been developed yet.

Herein, we develop a simple one-step and bottom-up wet-chemistry method to grow nanosized, ultrathin ternary $Mo_xW_{1-x}S_2$ nanosheets with good stability and a high metallic phase concentration on a gram-scale level. The Mo/W ratio was tuned by adjusting the growth parameters. Subsequently, the atom-scale structure and chemical states in the as-prepared electrocatalysts were characterized using high-angle annular dark field-scanning transmission electron microscopy (HAADF-STEM), X-ray absorption fine structure (XAFS), and X-ray photoelectron spectroscopy (XPS). Interestingly, the $Mo_{0.75}W_{0.25}S_2$ nanosheets, with the largest interlayer spacing of ~ 10.35 Å, exhibited the most efficient HER performance in acidic media. The enhancement mechanism, as observed through density functional theory (DFT) calculations, is also discussed, and the hydrogen-binding energy G_{H^*} on ternary $Mo_{0.75}W_{0.25}S_2$ was closer to the optimal value (G_{H^*} = 0) than that of 1T′-type MoS_2 and WS_2.

2 Experimental

2.1 Synthesis of the ultrathin $Mo_{1-x}W_xS_2$ nanosheets

The synthesis method was as follows: In a typical

experiment, x mmol of tungsten chloride (WCl_6, ≥ 99.99%, Sigma-Aldrich), y mmol of molybdenum chloride ($MoCl_5$, ≥ 99.99% Sigma-Aldrich) ($x + y = 1.0$, $x = 0.4$–0.9), and 6 mmol of thioacetamide (CH_3CSNH_2, ≥ 99.0%, TAA) were dissolved in 40 mL of a solvent mixture consisting of N,N-dimethyl formamide (DMF, ≥ 99.5%) and distilled water (> 10 MΩ) (v/v = 3:1) and stirred for 1 h at room temperature to obtain a homogeneous dispersion. The solution was then transferred to a 50-mL Teflon-lined stainless steel autoclave, heated to 210 ℃, and maintained at this temperature for 24 h. After cooling to room temperature, the product was washed several times with absolute alcohol (AR, ≥ 99.7%) and dried in a vacuum oven at 60 ℃ overnight.

2.2 Materials characterization

Samples were characterized using powder X-ray powder diffraction (PXRD) with a Philips X'Pert Pro Super diffractometer equipped with Cu Kα radiation (λ = 1.54178 Å). Their morphologies were determined using field-emission scanning electron microscopy (FE-SEM) (JEOL JSM-6700F SEM), transmission electron microscopy (TEM) (JEM-2100F) with an acceleration voltage of 200 kV, and HAADF-STEM using a JEOL JEM-ARF200F electron microscope (200 kV) with a spherical aberration corrector. Energy-dispersive X-ray spectroscopy (EDS) and elemental mapping were also performed. W L_3-edge and Mo K-edge XAFS spectra were collected at the Shanghai Synchrotron Radiation Facility (BL14W1, SSRF) and the Beijing Synchrotron Radiation Facility (1W1B, BSRF). The X-ray was monochromatized by a double-crystal Si (311) monochromator for SSRF and an Si (111) monochromator for BSRF, respectively. The monochromator was detuned to reject higher harmonics. The acquired extended XAFS (EXAFS) data were processed according to standard procedures using the WinXAS3.1 program [44]. Theoretical amplitudes and phase-shift functions were calculated with the FEFF8.2 code [45] using the crystal structural parameters of MoS_2 and WS_2. Raman spectra were measured using a Renishaw RM3000 Micro-Raman platform with a 532-nm laser. XPS measurements were carried out with a Thermo ESCALAB 250 X-ray photoelectron spectrometer equipped with an Mg Kα = 1,253.6 eV source. The binding energies of the XPS spectral range were calibrated for specimen charging effects using the C 1s level at an energy of 284.5 eV as a reference. UV–VIS–NIR absorption spectra were recorded with a Perkin Elmer Lambda 950 UV-VIS-NIR spectrophotometer. Element distribution was measured using inductively coupled plasma mass spectroscopy (ICP-MS) using an Optima 7300DV.

2.3 Electrochemical measurements

Electrocatalytic measurements were carried out using a standard three-electrode electrochemical workstation, and 0.5 M sulfuric acid (H_2SO_4, 70 mL, N_2-saturated) solution was used as the electrolyte. Carbon rod and Ag/AgCl electrodes (Pine Research Instrument, saturated with 3.5 M KCl) were used as the counter electrode and the reference electrode, respectively. The reference electrode was calibrated with respect to the reversible hydrogen electrode (RHE) using Pt sheets as the working and counter electrodes. In 0.5 M H_2SO_4, $E_{RHE} = E_{Ag/AgCl} + 0.2045$ V. Normally, 4 mg of $Mo_{1-x}W_xS_2$ powder was dissolved into a solvent mixture consisting of distilled water (0.75 mL) and isopropyl alcohol (0.25 mL), and 20 μL of a 5% Nafion solution was added to form a uniform ink after sonication. The ink then was loaded onto the glassy carbon electrode (GCE, 3 mm in diameter) at a mass loading of ~ 0.27 mg/cm^2 (~ 5 μL). Cyclic voltammetry (CV) was then carried out with scan rates of 20, 40, 60, 80, 100, 120, 140, 160, 180, and 200 mV/s in the potential range from 0.10 to 0.30 V (vs. RHE) to estimate the electrochemical double-layer capacitances to obtain the electrochemical active surface area. Linear sweep voltammetry (LSV) was then performed from 0.05 to –0.30 V (vs. RHE) with a scan rate of 2 mV/s using a CHI 660E electrochemical workstation. Each working electrode was cycled for at least 200 cycles prior to any measurements. The Nyquist plots were measured at frequencies ranging from 10^5 to 0.01 Hz at an overpotential of –200 mV (vs. RHE) with an amplitude voltage of 5 mV. The I–t curve was measured for 24 h after CV activation (over 500 cycles) at an overpotential of –0.175 V (vs. RHE) to investigate the electrochemical durability of the $Mo_{0.75}W_{0.25}S_2$ nanosheets in acidic solution. All LSV curves were obtained without iR correction.

2.4 Theoretical calculations

All the simulations were carried out with a DFT method based on a plane-wave basis, implemented by the Vienna *ab initio* Simulation Package (VASP) [46]. The electron–ion interactions were treated with the projector augmented wave (PAW) method [47], and the Perdew–Burke–Ernzerhof (PBE) exchange and correlation functional developed by Perdew, Burke, and Ernzerhof was used [48]. An energy cutoff of 400 eV and a 5 × 7 × 5 k-point Monkhorst–Pack grid [49] was used for the static calculations with a 2 × 2 supercell. Slab models with a vacuum layer thickness of 20 Å were used, and interlayer ammonium ions were considered. The calculations for hydrogen adsorption were spin-polarized. The total energy and force convergence criteria were less than 10^{-5} eV and –0.01 eV/Å, respectively. A T′-type phase with a zigzag chain [50, 51] was used to simulate the distorted MoS_2, WS_2, and $Mo_{0.75}W_{0.25}S_2$. Based on the model used by Nørskov [52], the adsorption free energy of hydrogen was calculated as

$$\Delta G_{H^*} = \Delta E_{H^*} + \Delta E_{ZPE} - T\Delta S_H$$

where ΔE_{H^*} is the hydrogen chemisorption energy, ΔE_{ZPE} is the difference in the zero point energy, and $T\Delta S_H$ is the entropy contribution between the H-adsorbed state and H_2 in the gas phase. ΔS_H was replaced by $-1/2 \cdot S(H_2)$ at standard conditions of T = 298 K and pressure = 1 atm.

3 Results and discussion

3.1 Synthesis and characterization of the $Mo_{1-x}W_xS_2$ ultrathin nanosheets

In our experiments, gram-scale (Fig. S1 in the Electronic Supplementary Material (ESM)) metallic $Mo_{1-x}W_xS_2$ ultrathin nanosheets were synthesized through a facile bottom-up wet chemistry method; further details can be found in the experimental section. Figure 1(a) shows a typical TEM image of the obtained $Mo_{1-x}W_xS_2$ nanostructures, which exhibit a curly structure. In contrast, pure MoS_2 and WS_2 synthesized under the same conditions are likely to form aggregates or large sheets (Fig. S2 in the ESM). Furthermore, the coexistence of the elements Mo, W, and S was demonstrated from the EDS analysis; the copper signal originated from the copper substrate (Fig. S3 in the ESM). Elemental mapping of the $Mo_{1-x}W_xS_2$ nanosheets (Figs. 1(b)–1(e)) further indicates the homogeneous distribution of the elements Mo, W, and S throughout the entire samples. The high-resolution TEM (HRTEM) image of the $Mo_{1-x}W_xS_2$ nanosheets (Fig. 1(f)) shows many upright edges of layers (less than 5 layers) and a distinctly enlarged interlayer spacing of greater than 10 Å, revealing that a two-dimensional layered structure with an expanded layer spacing is obtained. To illustrate the structure clearly, we have depicted the simple layer structure in Fig. 1(g). Further elemental components and structural evidence will be given in following sections.

To confirm the chemical composition of the as-obtained $Mo_{1-x}W_xS_2$ nanosheets, we used ICP-MS. The detailed atomic ratios of several $Mo_{1-x}W_xS_2$ catalysts are listed (see Table S1 in the ESM), indicating that the value of x ranged from 0.11 to 0.60 in various samples. To explore the crystal structure of these samples, PXRD analysis was carried out. As can be seen in Fig. 2(a) and Fig. S4 in the ESM, the XRD patterns of the $Mo_{1-x}W_xS_2$ nanosheets synthesized with various ratios matched well with those of the metallic binary materials.

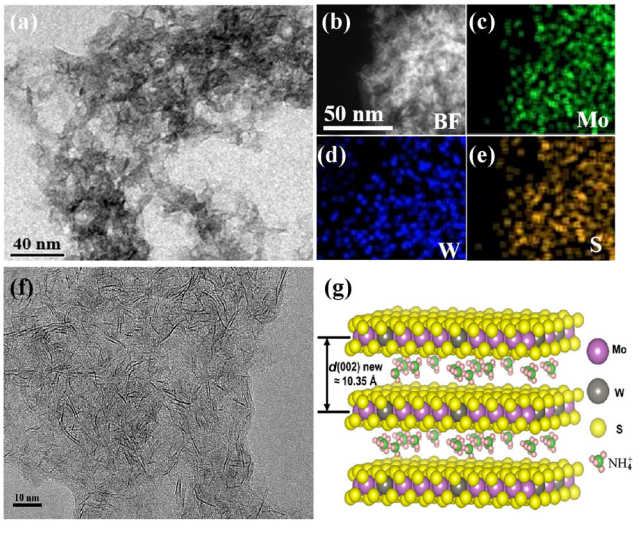

Figure 1 (a) TEM, and (b)–(e) element mapping images of metallic ultrathin $Mo_{0.75}W_{0.25}S_2$ nanosheets, indicating the homogeneous distribution of Mo, W, and S. (f) HRTEM images of metallic ultrathin $Mo_{1-x}W_xS_2$ nanosheets with enlarged interlayer spacing. (g) A structural model of the $Mo_{1-x}W_xS_2$ layers with the intercalation of ammonium ions.

The most intense peak for each sample, centered at < 10°, is the (002) diffraction peak, which corresponds to the individual interlayer spacing value. This result is obviously different from that of the standard TMD structure in Fig. 2(a), but it is consistent with NH^{4+}-intercalated results [40, 41]. To prove the successful intercalation of NH^{4+} into the $Mo_{1-x}W_xS_2$ nanosheets, we performed differential scanning calorimetry (DSC, see Fig. S5 in the ESM), and the obvious desorption peak at ~ 230 ˚C matched well with our previous reports [40, 41]. For further verification, we measured the PXRD of the annealed sample (Fig. S6 in the ESM). Peak shift to high degree was observed, indicating decreased interlayer spacing after thermal annealing. It is worth noting that the annealed $Mo_{1-x}W_xS_2$ nanosheets also had an enlarged interlayer spacing (~ 0.67 nm) in contrast to that of annealed binary samples in our previous reports [40, 41]. Meanwhile, all as-prepared ternary and binary samples exhibited expanded spacing; values for the different samples are shown in Fig. 2(b). Here, the interplanar distance (d) is calculated from the Bragg formula: $2d\cdot\sin\theta = n\lambda$, where θ and λ represent the incidence angle and the X-ray wavelength (1.54178 Å), respectively. Most of the ternary $Mo_{1-x}W_xS_2$ nanosheets have an interlayer spacing of > 10 Å, which is consistent with the HRTEM result above. We suggest that ternary materials obtain a larger spacing than their binary counterparts, probably due to the distorted in-plane structure from the combined effects of heteroatoms and NH^{4+}-intercalation.

3.2 Electrocatalytic HER performance of the $Mo_{1-x}W_xS_2$ ultrathin nanosheets

To study the connection between the W/Mo ratio and catalytic activity, we evaluated the electrocatalytic water splitting performance of the as-obtained $Mo_{1-x}W_xS_2$ nanosheets using a standard three-electrode electrochemical testing apparatus in N_2-saturated 0.5 M H_2SO_4 solution (see detailed data in Experimental section). The total mass of the dropcasted $Mo_{1-x}W_xS_2$ nanosheets was quite small, and a thin black film was formed after drying at room temperature. The polarization curves with no *iR* correction, in which the area current density is plotted against the applied potential vs. the RHE, demonstrate the HER behavior of various $Mo_{1-x}W_xS_2$ nanosheets compared with 20% Pt/C (Fig. 3(a)). The highly crystalline WS_2 sample exhibited very inert HER activity, close to that of bulk WS_2, which was probably due to high resistance and a low number of exposed active sites (see Fig. 2(a), and Figs. S2(a), S7, S8(a) and S8(b) in the ESM). Similarly, highly agglomerated MoS_2 showed only slightly better performance (Figs. S2(b), S7, S8(c) and S8(d) in the ESM). Interestingly, when the heteroatom was introduced into MX_2 products (M = Mo, W), their electrocatalytic activity was dramatically enhanced, as proved by their higher catalytic current and lower overpotentials. For instance, the $Mo_{0.75}W_{0.25}S_2$ nanosheets showed the best performance, exhibiting a very low onset potential of –96 mV vs. RHE before correcting for *iR* losses. Moreover, an applied potential of only –155 mV vs. RHE was required to obtain an electrocatalytic current density of –10 mA/cm^2, which is slightly superior to any previous reports (see Table S2 in the ESM). However, further increasing or decreasing the W content to greater to or less than x = 0.25 resulted in fading of the HER behavior to a large extent, as seen in Fig. 3(a). This fading probably resulted from combined effects

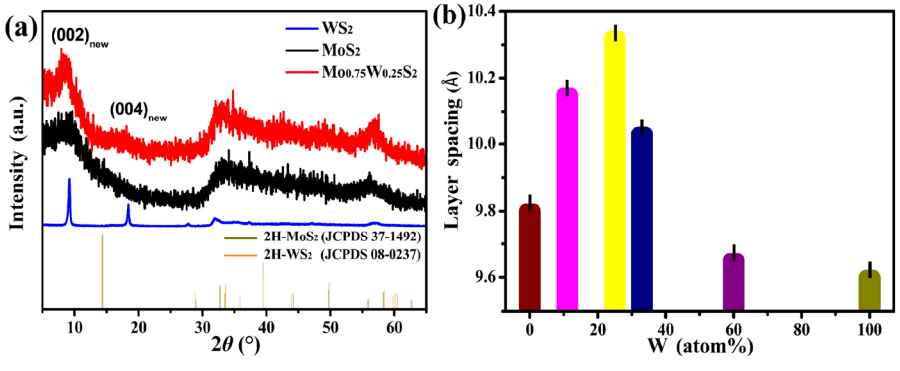

Figure 2 (a) XRD patterns of $Mo_{0.75}W_{0.25}S_2$ nanosheets compared with their binary counterparts. (b) Corresponding interlayer spacing calculated from XRD data.

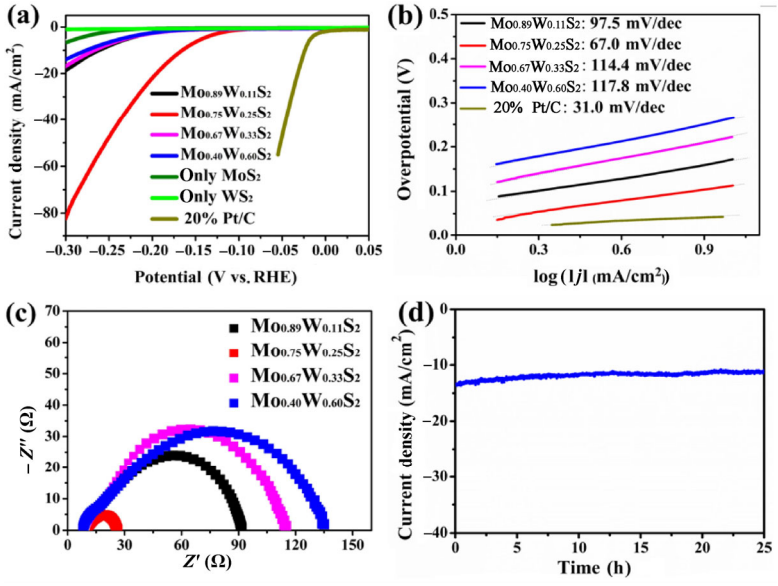

Figure 3 (a) Polarization curves and (b) corresponding Tafel slopes of several $Mo_{1-x}W_xS_2$ nanosheets prepared with different atomic ratios, and of commercial 20% Pt/C catalyst. (c) Nyquist plots of various samples over the frequency range from 10^5 to 0.01 Hz at a set overpotential. (d) *I*–*t* curve obtained at overpotential η = 175 mV vs. RHE for 25 h in 0.5 M H_2SO_4.

of changes in the interlayer spacing, exposed active area, and metallic phase concentration. Additionally, we suppose that these variables would have interrelated effects on the electrochemical activity of the catalysts; the expanded spacing would weaken the interlaminar force to nearly single layer nature and simultaneously distort the in-plane arrangement, thus enhancing the metallic property and increasing the number of surface active sites.

The high intrinsic HER performance of the $Mo_{0.75}W_{0.25}S_2$ nanosheets (x = 0.25) was further assessed by calculating their Tafel slopes. Tafel analysis demonstrated that the incorporation of W from a suitable source significantly decreased the slope to 67 mV/dec, which was smaller than that of the samples with any other ratios. This indicated that the HER moved to a Volmer–Heyrovsky pathway, which is one of the more favorable mechanisms for electrocatalytic hydrogen evolution, with a fast discharge reaction ($H_3O^+ + e^- \rightarrow H_{ads} + H_2O$) and desorption process ($H_{ads} + H_3O^+ + e^- \rightarrow H_2 + H_2O$) (Fig. 3(b)). In addition, rapid charge transfer is critical for HER performance. We performed electrochemical impedance spectroscopy (EIS) at a set overpotential to investigate the electrode kinetics in HER. The experimental data is shown in Fig. 3(c). In the Nyquist plots of all materials, only four semicircles are observed, except for the typical Warburg impedances, indicating that mass transport is sufficiently rapid, and the reaction is kinetically controlled. For comparison, the EIS of binary materials showed impedances much greater than those of the ternary samples (Fig. S7 in the ESM). As compared to the samples with different ratios, the $Mo_{0.75}W_{0.25}S_2$ nanosheets had lower charge transfer resistance ($R_{ct} \approx 15$ vs. 84, 107, and 126 Ω for x = 0.11, x = 0.33, and x = 0.60, respectively, obtained from the intercept at the x-axis), corresponding to very favorable charge transfer kinetics with effective transport and a decreased recombination rate. The difference in the HER performance of these five catalysts could also be attributed to their electrochemically active surface area. We evaluated the relative number of active sites from the electrochemical double-layer capacitance (EDLC), calculated from the data of capacitive current vs. scan rate. As shown in Fig. S9 in the ESM, all the CV curves had a slightly distorted rectangular shape, implying an EDLC-dominated process. The $Mo_{0.75}W_{0.25}S_2$ nanosheets had the largest EDLC value, ~ 9.42 mF/cm², compared to the other three samples (4.24 mF/cm², for x = 0.11, x = 0.33, and x = 0.60, respectively), demonstrating its larger active area. The EDLC values of the corresponding binary materials demonstrated obviously smaller active

areas (Fig. S8 in the ESM). The ideal surface of the $Mo_{0.75}W_{0.25}S_2$ nanosheets may play a key role in their different HER behavior, which is similar to the result reported by Jin and co-authors [53]. Furthermore, electrochemical stability, a very important criterion in judging HER performance, is necessary for any electrode material. To probe the durability of $Mo_{1-x}W_xS_2$ nanosheets in acidic surroundings, their long-term stability was assessed over 24 h under a constant potential. It is noteworthy that, as shown in Fig. 3(d), the current density declined only negligibly for our sample, and always retained almost 90% after long-term testing.

3.3 Detailed measurements of the atomic structure of the ultrathin $Mo_{1-x}W_xS_2$ nanosheets

To confirm that the $Mo_{1-x}W_xS_2$ nanosheets had a local distorted structure, synchrotron-radiation-based XAFS was carried out, as shown in Fig. 4. XAFS can investigate the coordination surroundings and the local bond lengths of a given component as central atom. Figure 4(a) shows the oscillation function curves of the W L_3-edge in the k range 3–11.5 $Å^{-1}$ for four different $Mo_{1-x}W_xS_2$ nanosheets with different x values in contrast with a foil sample. The $\kappa^3\chi(k)$ of these $Mo_{1-x}W_xS_2$ nanosheets are significantly different from that of the foil, indicating a remarkable change in the local atomic arrangements. Furthermore, the Fourier transform (FT) spectra in real space can identify the nature of this alteration. As shown in Fig. 4(b), the FT curve of the foil is characterized by two main peaks at ~ 2.00 and ~ 2.86 Å, corresponding to the nearest W–S and W–W bonds from the first and second shell, respectively. In contrast, the FT curves of $Mo_{1-x}W_xS_2$ nanosheets indicate that the intensity of all peaks decreased, probably owing to the presence of many defects due to the solvothermal synthesis method. Furthermore, the lengths of the nearest metal–metal bonds noticeably shifted from ~ 2.86 to ~ 2.67 Å. The decreased bonding length strongly demonstrates the distorted structure. Similarly, obvious shifts of the Mo K-edge were observed (Figs. 4(c) and 4(d)). A noticeable alteration was also seen in the X-ray absorption near-edge spectroscopy (XANES) (Fig. S10 in the ESM). The quantitative structural results of the different $Mo_{1-x}W_xS_2$ nanosheets

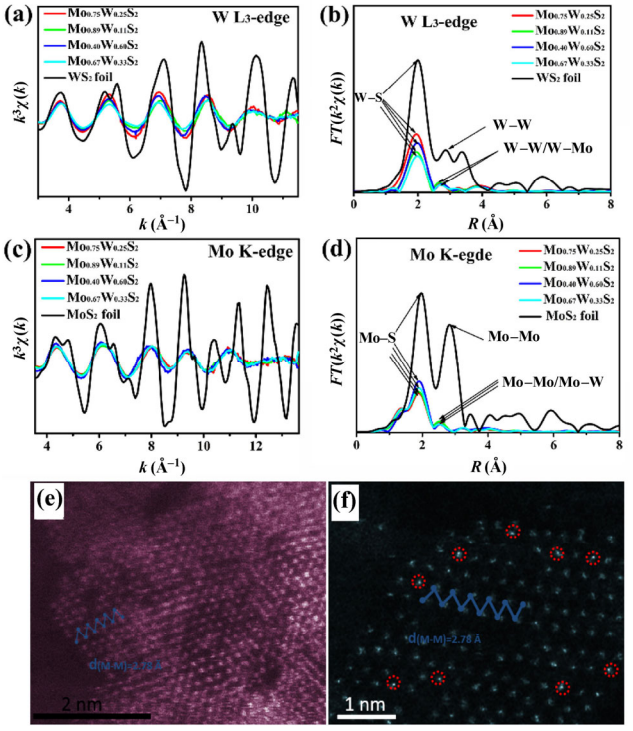

Figure 4 (a) The synchrotron-radiation-based XAFS spectra showing the W L_3-edge oscillation functions $\kappa^3\chi(k)$ and (b) the corresponding FT spectra in real space. (c) Mo K-edge oscillation functions $\kappa^3\chi(k)$ and (d) the corresponding FT analysis. (e) and (f) Typical HAADF-STEM images of $Mo_{0.75}W_{0.25}S_2$ nanosheets. These results clearly confirm the distorted metal–metal bonds in the $Mo_{1-x}W_xS_2$ nanosheets and coexistence of heteroatoms.

were fitted from the EXAFS data and summarized (see Table S3 in the ESM), using the ARTEMIS module of IFEFFIT and the USTCXAFS software package.

The direct observation of the atomic arrangement was explored using the high-resolution HAADF-STEM images in Figs. 4(e) and 4(f). As shown, unique zigzag-chain lattices with a nearest metal–metal distance of 2.78 Å were achieved, which is similar to that of metallic binary TMDs we have reported, but distinctively shorter than that for 2H-phase TMDs [40, 41]. Additionally, two kinds of atoms with different brightness were present, and several brighter atoms are highlighted using a red dotted circle. This effect is probably caused by the Mo and W atoms, due to their different atomic numbers (Fig. 4(f)). Clearly, the parsed bond length was in agreement with the observation in Figs. 4(e) and 4(f). The distorted structure could be further confirmed from the Raman scattering features. In Fig. S11 in the ESM, each sample displays

two obvious peaks, corresponding to E^1_{2g} and A_{1g} features, respectively, which correspond to TMDs with 2H structure. Meanwhile, all materials showed additional Raman features in the low-frequency region. These additional peaks in the different samples can be explained by the existence of a distorted zigzag-chain superlattice, which is in agreement with the observations from XAFS and HAADF-STEM. It is worth noting that $Mo_{0.75}W_{0.25}S_2$ showed relatively stronger peaks at low frequency (dotted area) than others, which to some extent reveals that the concentration of the distorted structure was higher in our as-obtained sample. To summarize, the existence of the distorted in-plane superlattice structure was confirmed from the changes in the atomic arrangement that we detected.

3.4 Metallic phase concentration of different ultrathin $Mo_{1-x}W_xS_2$ nanosheets

The distorted superlattice structure in TMD would lead to the existence of a metallic phase. To directly determine the chemical states, and even the metallic phase concentration and optical absorption properties for the $Mo_{1-x}W_xS_2$ nanosheets, we characterized them using XPS and UV–VIS–NIR spectra. The XPS survey data (see Fig. S12 in the ESM) revealed the coexistence of Mo, W, S, and N. Figures 5(a)–5(c) show the high-resolution XPS spectra of the Mo 3d, W 4f, and S 2p signals, respectively. In these visual regions, the signals of the bulk crystal occurred at 229.1 and 232.2 eV (green lines), corresponding to the Mo^{4+} $3d_{5/2}$ and Mo^{4+} $3d_{3/2}$ of 2H-MoS_2. For the $Mo_{1-x}W_xS_2$ nanosheets, two peaks appeared at 229.1 and 232.2 eV, indicating the presence of a partial semiconductor phase. However, it is notable that two main peaks located at 228.1 and 231.1 eV with a large shift in their binding energy (~ 1.0 eV) appeared (red lines). Moreover, similar downward shifts for W 4f and S 2p can also be observed. These results are consistent with the previously reported metallic nature of chemically exfoliated Mo/W-based MX_2 materials [33, 34, 42]. Therefore, all the analyses of the XPS spectra directly demonstrated the presence of a metallic phase in the ultrathin $Mo_{1-x}W_xS_2$ nanosheets. The metallic phase concentration in these nanosheets was further calculated based on the Mo 3d spectra (Fig. 5(a) and Figs. S13(a)–S13(c) in the ESM).

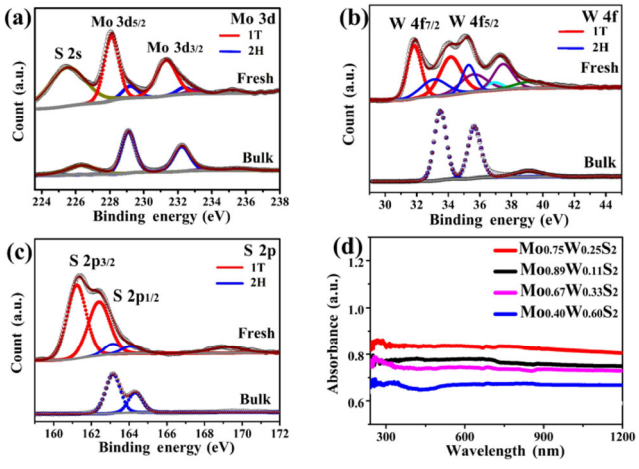

Figure 5 (a)–(c) High-resolution XPS spectra of Mo 3d, W 4f, and S 2p core level peak regions of the as-prepared $Mo_{0.75}W_{0.25}S_2$ nanosheets, respectively. (d) UV–VIS–NIR spectra for various $Mo_{1-x}W_xS_2$ nanosheet powders.

The diverse metallic phase concentration (54%–90%) was obviously reflected in the XPS spectra. The catalytic behavior of these nanosheets is affected mainly by this difference, which will be summarized later. The metallic property of $Mo_{1-x}W_xS_2$ nanosheets was further confirmed by the absorption spectra (Fig. 5(d)), in which characteristic signals of metallic species, exhibiting intense total absorbance over a large wavelength range, can be observed.

3.5 Relationship between HER and metallic phase concentration

In Fig. 6(a), we summarize the relationships between the W atom ratio (%), metallic phase concentration, and overpotential at 5 mA/cm^2. A near-linear relationship between the metallic phase concentration and potential at 5 mA/cm^2 can be seen, which to some degree indicates that the excellent HER performance could be attributed to the metallic property and intrinsic activity. Interestingly, the controlled incorporation of W optimized the metallic phase ratio in $Mo_{1-x}W_xS_2$ nanosheets. $Mo_{0.75}W_{0.25}S_2$ showed the best catalytic behavior among our prepared materials. To gain an in-depth understanding of the catalytic activity of these $Mo_{1-x}W_xS_2$ nanosheets, the hydrogen turnover frequency (TOF) values calculated from the EDLC and polarization curves are shown in Fig. 6(b). The $Mo_{0.75}W_{0.25}S_2$ nanosheets had a TOF of 0.3 H_2 per

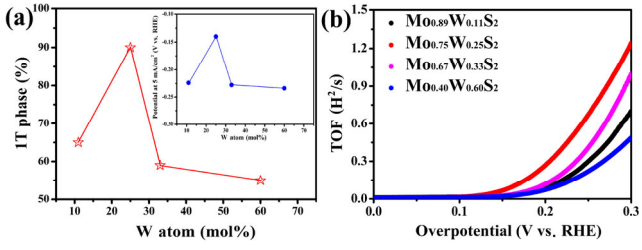

Figure 6 The relationship between HER and metallic phase concentration. (a) The connection between W content, metallic phase concentration, and overpotential at j = 5 mA/cm^2. (b) The TOF of different samples calculated from the EDLC and polarization curves.

second and 1.3 H_2 per second at overpotentials –200 and –300 mV vs. RHE, respectively, which are the highest values among these catalysts. The exchange current density (J_{ex}), one of the most important electrochemical parameters, to some degree intuitively reflects the kinetic activity and the reversibility of the electrode reaction. Here, J_{ex} was obtained by the extrapolation of the Tafel slopes (see Fig. S14(a) in the ESM). The $Mo_{0.75}W_{0.25}S_2$ nanosheets displayed a large J_{ex} of 92 μA/cm^2, indicating the lower barrier from kinetics and the high-performance electrode reaction. For direct comparison, the concentration of the metallic phase vs. J_{ex} is shown in Fig. S14(b) in the ESM, and an obvious advantage was exhibited for the $Mo_{0.75}W_{0.25}S_2$ nanosheets.

3.6 The first-principles calculations

Taking the above-mentioned analyses into account, to further investigate the feasibility of $Mo_{1-x}W_xS_2$ as HER catalysts, first-principles calculations were performed (see computational details in Experimental section). Pure metallic WS_2, MoS_2, and $Mo_{0.75}W_{0.25}S_2$ with interlayer ammonium ions and distorted T-type structures (1T′ phase) were used as models (Fig. S15 in the ESM). The calculated band structures of WS_2, MoS_2, and $Mo_{0.75}W_{0.25}S_2$ are depicted in Fig. 7(a)–7(c), confirming the observed metallic behaviors in the experiments. The Gibbs free energy, which is considered an important factor in the evaluation of HER activity, should be zero for an optimum intermediate state. To compare the theoretical performance of the materials, the Gibbs free energies were calculated (Fig. 7(d) and Table S4 in the ESM). The calculation results indicated poor electrocatalytic HER performance of WS_2 compared with MoS_2. The free energy of pure WS_2 is 0.332 eV, more positive than that of MoS_2 (0.242 eV). Notably, the optimized $Mo_{1-x}W_xS_2$ structure resulted in obviously improved adsorption–desorption behavior (0.119 eV) with enhanced HER kinetics compared to metallic MoS_2. From this, we can conclude that the metallic $Mo_{0.75}W_{0.25}S_2$ can be regarded as an excellent HER catalyst based on theoretical calculations. The enhanced

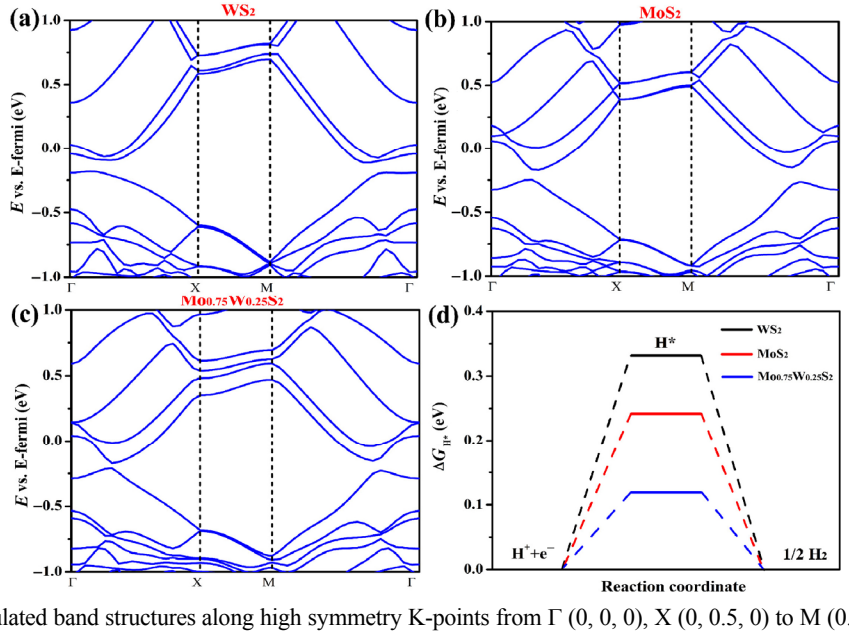

Figure 7 (a)–(c) Calculated band structures along high symmetry K-points from Γ (0, 0, 0), X (0, 0.5, 0) to M (0.5, 0.5, 0). (d) Calculated free energy diagram of adsorbed hydrogen on the surfaces of WS_2, MoS_2 and $Mo_{0.75}W_{0.25}S_2$.

catalytic performance of $Mo_{1-x}W_xS_2$ relative to MoS_2 also demonstrates the advantage of ternary metallic $Mo_{0.75}W_{0.25}S_2$ in HER. In brief, this result highlights the significance of our work in the field of synthesis of high metallic phase concentration LTMDs, and the vital role of metallic features in HER catalysis.

4 Conclusions

In summary, a simple bottom-up method for the large-scale synthesis of high-metallic-phase-concentration ultrathin $Mo_{1-x}W_xS_2$ nanosheets with enlarged interlayer spacing was developed. The electrocatalytic HER activity of $Mo_{1-x}W_xS_2$ can be modulated by controlling the ratio of the components. Detailed characterization revealed that the favorable kinetics, metallic conductivity, and large exposed active surface area could enable better HER performance in $Mo_{1-x}W_xS_2$ with expanded interlayer spacing. Notably, the optimized $Mo_{0.75}W_{0.25}S_2$ nanosheets exhibited excellent cycling stability and interesting HER behavior, with the lowest overpotential of –0.155 V at –10 mA/cm^2 (not *iR* corrected) and the smallest Tafel slope of 67 mV/dec, as compared to $Mo_{1-x}W_xS_2$ with other x values. This method provides a simple approach to mass-produce low-cost and highly active two-dimensional layered catalysts with high metallic phase concentration, thus opening the door to further exploration of their specific applications.

Acknowledgements

We acknowledge the financial support of the National Basic Research Program of China (Nos. 2014CB848900 and 2016YFA0200602), the National Natural Science Foundation of China (Nos. U1532112, 11375198, 11574280, and 21573204), CUSF (No. WK2310000053) and funds from Key Laboratory of Advanced Energy Materials Chemistry (Ministry of Education). L. S. thanks the recruitment program of global experts, the CAS Hundred Talent Program. We also thank the Shanghai synchrotron Radiation Facility (14W1, SSRF), the Beijing Synchrotron Radiation Facility (1W1B and soft-X-ray endstation, BSRF), the Hefei Synchrotron Radiation Facility (MCD and Photoemission Endstations, NSRL) and USTC Center for Micro and Nanoscale Research and Fabrication.

Electronic Supplementary Material: Supplementary material (optical images, SEM images, EDS spectrum, XRD patterns, DSC, XAFS, Raman, XPS, ICP, and images from DFT calculations and auxiliary electrochemical data) is available in the online version of this article at https://doi.org/10.1007/s12274-017-1786-x.

References

[1] Karunadasa, H. I.; Chang, C. J.; Long, J. R. A molecular molybdenum-oxo catalyst for generating hydrogen from water. *Nature* **2010**, *464*, 1329–1333.

[2] Walter, M. G.; Warren, E. L.; McKone, J. R.; Boettcher, S. W.; Mi, Q. X.; Santori, E. A.; Lewis, N. S. Solar water splitting cells. *Chem. Rev.* **2010**, *110*, 6446–6471.

[3] Dresselhaus, M. S.; Thomas, I. L. Alternative energy technologies. *Nature* **2001**, *414*, 332–337.

[4] Turner, J. A. Sustainable hydrogen production. *Science* **2004**, *305*, 972–974.

[5] Zhao, Y.; Kamiya, K.; Hashimoto, K.; Nakanishi, S. *In situ* CO_2-emission assisted synthesis of molybdenum carbonitride nanomaterial as hydrogen evolution electrocatalyst. *J. Am. Chem. Soc.* **2015**, *137*, 110–113.

[6] Zheng, Y.; Jiao, Y.; Zhu, Y. H.; Li, L. H.; Han, Y.; Chen, Y.; Du, A. J.; Jaroniec, M.; Qiao, S. Z. Hydrogen evolution by a metal-free electrocatalyst. *Nat. Commun.* **2014**, *5*, 3783.

[7] Stamenkovic, V. R.; Mun, B. S.; Arenz, M.; Mayrhofer, K. J. J.; Lucas, C. A.; Wang, G. F.; Ross, P. N.; Markovic, N. M. Trends in electrocatalysis on extended and nanoscale Pt-bimetallic alloy surfaces. *Nat. Mater.* **2007**, *6*, 241–247.

[8] Dempsey, J. L.; Brunschwig, B. S.; Winkler, J. R.; Gray, H. B. Hydrogen evolution catalyzed by cobaloximes. *Acc. Chem. Res.* **2009**, *42*, 1995–2004.

[9] Xie, J. F.; Zhang, J. J.; Li, S.; Grote, F. B.; Zhang, X. D.; Zhang, H.; Wang, R. X.; Lei, Y.; Pan, B. C.; Xie, Y. Controllable disorder engineering in oxygen-incorporated MoS_2 ultrathin nanosheets for efficient hydrogen evolution. *J. Am. Chem. Soc.* **2013**, *135*, 17881–17888.

[10] Xing, Z. C.; Yang, X. R.; Asiri, A. M.; Sun, X. P. Three-dimensional structures of MoS_2@Ni core/shell nanosheets array toward synergetic electrocatalytic water splitting. *ACS Appl. Mater. Interface* **2016**, *8*, 14521–14526.

[11] Kong, D. S.; Wang, H. T.; Lu, Z. Y.; Cui, Y. $CoSe_2$ nanoparticles grown on carbon fiber paper: An efficient and stable electrocatalyst for hydrogen evolution reaction. *J. Am. Chem. Soc.* **2014**, *136*, 4897–4900.

[12] Faber, M. S.; Jin, S. Earth-abundant inorganic electrocatalysts and their nanostructures for energy conversion applications. *Energy Environ. Sci.* **2014**, *7*, 3519–3542.

[13] Li, Y. H.; Liu, P. F.; Pan, L. F.; Wang, H. F.; Yang, Z. Z.; Zheng, L. R.; Hu, P.; Zhao, H. J.; Gu, L.; Yang, H. G. Local atomic structure modulations activate metal oxide as electrocatalyst for hydrogen evolution in acidic water. *Nat. Commun.* **2015**, *6*, 8064.

[14] Popczun, E. J.; McKone, J. R.; Read, C. G.; Biacchi, A. J.; Wiltrout, A. M.; Lewis, N. S.; Schaak, R. E. Nanostructured nickel phosphide as an electrocatalyst for the hydrogen evolution reaction. *J. Am. Chem. Soc.* **2013**, *135*, 9267–9270.

[15] Vrubel, H.; Hu, X. L. Molybdenum boride and carbide catalyze hydrogen evolution in both acidic and basic solutions. *Angew. Chem., Int. Ed.* **2012**, *124*, 12875–12878.

[16] Peng, S. J.; Li, L. L.; Han, X. P.; Sun, W. P.; Srinivasan, M.; Mhaisalkar, S. G.; Cheng, F. Y.; Yan, Q. Y.; Chen, J.; Ramakrishna, S. Cobalt sulfide nanosheet/graphene/carbon nanotube nanocomposites as flexible electrodes for hydrogen evolution. *Angew. Chem., Int. Ed.* **2014**, *126*, 12802–12807.

[17] Voiry, D.; Yamaguchi, H.; Li, J. W.; Silva, R.; Alves, D. C. B.; Fujita, T.; Chen, M. W.; Asefa, T.; Shenoy, V. B.; Eda, G. et al. Enhanced catalytic activity in strained chemically exfoliated WS_2 nanosheets for hydrogen evolution. *Nat. Mater.* **2013**, *12*, 850–855.

[18] Ye, R. Q.; del Angel-Vicente, P.; Liu, Y. Y.; Arellano-Jimenez, M. J.; Peng, Z. W.; Wang, T.; Li, Y. L.; Yakobson, B. I.; Wei, S. H.; Yacaman, M. J. et al. High-performance hydrogen evolution from $MoS_{2(1-x)}P_x$ solid solution. *Adv. Mat.* **2016**, *28*, 1427–1432.

[19] Chhowalla, M.; Shin, H. S.; Eda, G.; Li, L. J.; Loh, K. P.; Zhang, H. The chemistry of two-dimensional layered transition metal dichalcogenide nanosheets. *Nat. Chem.* **2013**, *5*, 263–275.

[20] Zeng, Z. Y.; Tan, C. L.; Huang, X.; Bao, S. Y.; Zhang, H. Growth of noble metal nanoparticles on single-layer TiS_2 and TaS_2 nanosheets for hydrogen evolution reaction. *Energy Environ. Sci.* **2014**, *7*, 797–803.

[21] Tan, C. L.; Zhang, H. Two-dimensional transition metal dichalcogenide nanosheet-based composites. *Chem. Soc. Rev.* **2015**, *44*, 2713–2731.

[22] Merki, D.; Fierro, S.; Vrubel, H.; Hu, X. L. Amorphous molybdenum sulfide films as catalysts for electrochemical hydrogen production in water. *Chem. Sci.* **2011**, *2*, 1262–1267.

[23] Voiry, D.; Yang, J.; Chhowalla, M. Recent strategies for improving the catalytic activity of 2D TMD nanosheets toward the hydrogen evolution reaction. *Adv. Mater.* **2016**, *28*, 6197–6206.

[24] Yu, Y. F.; Huang, S. Y.; Li, Y. P.; Steinmann, S. N.; Yang, W. T.; Cao, L. Y. Layer-dependent electrocatalysis of MoS_2 for hydrogen evolution. *Nano Lett.* **2014**, *14*, 553–558.

[25] Zhao, X.; Ma, X.; Sun, J.; Li, D. H.; Yang, X. R. Enhanced catalytic activities of surfactant-assisted exfoliated WS_2 nanodots for hydrogen evolution. *ACS Nano* **2016**, *10*, 2159–2166.

[26] Merki, D.; Hu, X. L. Recent developments of molybdeuum and tungsten sulfides as hydrogen evolution catalysts. *Energy Environ. Sci.* **2011**, *4*, 3878–3888.

[27] He, J. N.; Liang, Y. Q.; Mao, J.; Zhang, X. M.; Yang, X. J.; Cui, Z. D.; Zhu, S. L.; Li, Z. Y.; Li, B. B. 3D tungsten-doped MoS_2 nanostructure: A low-cost, facile prepared catalyst for hydrogen evolution reaction. *J. Electrochem. Soc.* **2016**, *163*, H299–H304.

[28] Wang, L.; Sofer, Z.; Luxa, J.; Pumere, M. $Mo_xW_{1-x}S_2$ solid solutions as 3D electrodes for hydrogen evolution reaction. *Adv. Mater. Interfaces* **2015**, *2*, 1500041.

[29] Zhang, X. W.; Meng, F.; Mao, S.; Ding, Q.; Shearer, M. J.; Faber, M. S.; Chen, J. H.; Hamers, R. J.; Jin, S. Amorphous MoS_xCl_y electrocatalysts supported by vertical graphene for efficient electrochemical and photoelectrocemical hydrogen generation. *Energy Environ. Sci.* **2015**, *8*, 862–868.

[30] Fu, Q.; Yang, L.; Wang, W. H.; Han, A. L.; Huang, J.; Du, P. W.; Fan, Z. Y.; Zhang, J. Y.; Xiang, B. Synthesis and enhanced electrochemical catalytic performance of monolayer $WS_{2(1-x)}Se_{2x}$ with a tunable band gap. *Adv. Mater.* **2015**, *27*, 4732–4738.

[31] Gong, Q. F.; Cheng, L.; Liu, C. H.; Zhang, M.; Feng, Q. L.; Ye, H. L.; Zeng, M.; Xie, L. M.; Liu, Z.; Li, Y. G. Ultrathin $MoS_{2(1-x)}Se_{2x}$ alloy nanoflakes for electrocatalytic hydrogen evolution reaction. *ACS Catal.* **2015**, *5*, 2213–2219.

[32] Kibsgaard, J.; Chen, Z. B.; Reinecke, B. N.; Jaramillo, T. F. Engineering the surface structure of MoS_2 to preferentially expose active edge sites for electrocatalysis. *Nat. Mater.* **2012**, *11*, 963–969.

[33] Cai, Y.; Yang, X.; Liang, T.; Dai, L.; Ma, L.; Huang, G. W.; Chen, W. X.; Chen, H. Z.; Su, H. X.; Xu, M. S. Easy incorporation of single-walled carbon nanotubes into two-dimensional MoS_2 for high-performance hydrogen evolution. *Nanotechnology* **2014**, *25*, 465401.

[34] Duan, J. J.; Chen, S.; Chambers, B. A.; Andersson, G. G.; Qiao, S. Z. 3D WS_2 nanolayers@heteroatom-doped graphene films as hydrogen evolution catalyst electrodes. *Adv. Mater.* **2015**, *27*, 4234–4241.

[35] Wypych, F.; Solenthaler, C.; Prins, R.; Weber, Th. Electron diffraction study of intercalation compounds derived from 1T-MoS_2. *J. Solid State Chem.* **1999**, *144*, 430–436.

[36] Lukowski, M. A.; Daniel, A. S.; English, C. R.; Meng, F.; Forticaux, A.; Hamers, R. J.; Jin, S. Highly active hydrogen evolution catalysis from metallic WS_2 nanosheets. *Energy Environ. Sci.* **2014**, *7*, 2608–2613.

[37] Lukowski, M. A.; Daniel, A. S.; Meng, F.; Forticaux, A.; Li, L. S.; Jin, S. Enhanced hydrogen evolution catalysis from chemically exfoliated metallic MoS_2 nanosheets. *J. Am. Chem. Soc.* **2013**, *135*, 10274–10277.

[38] Voiry, D.; Salehi, M.; Silva, R.; Fujita, T.; Chen, M. W.; Asefa, T.; Shenoy, V. B.; Eda, G.; Chhowalla, M. Conducting MoS_2 nanosheets as catalysts for hydrogen evolution reaction. *Nano Lett.* **2013**, *13*, 6222–6227.

[39] Wypych. F.; Schöllhorn, R. 1T-MoS_2, a new metallic modification of molybdenum disulfide. *J. Chem. Soc. Chem. Commun.* **1992**, 1386–1388.

[40] Liu, Q.; Li, X. L.; Xiao, Z. R.; Zhou, Y.; Chen, H. P.; Khalil, A.; Xiang, T.; Xu, J. Q.; Chu, W. S.; Wu, X. J. et al. Stable metallic 1T-WS_2 nanoribbons intercalated with ammonia ions: The correlation between structure and electrical/optical properties. *Adv. Mater.* **2015**, *27*, 4837–4844.

[41] Liu, Q.; Li, X. L.; He, Q.; Khalil, A.; Liu, D. B.; Xiang, T.; Wu, X. J.; Song, L. Gram-scale aqueous synthesis of stable few-layered 1T-MoS_2: Applications for visible-light-driven photocatalytic hydrogen evolution. *Small* **2015**, *11*, 5556–5564.

[42] Liu, Q.; Sun, C. Y.; He, Q.; Khalil, A.; Xiang, T.; Liu, D. B.; Zhou, Y.; Wang, J.; Song, L. Stable metallic 1T-WS_2 ultrathin nanosheets as a promising agent for near-infrared photothermal ablation cancer therapy. *Nano Res.* **2015**, *8*, 3982–3991.

[43] Wang, F. M.; Li, J. S.; Wang, F.; Shifa, T. A.; Cheng, Z. Z.; Wang, Z. X.; Xu, K.; Zhan, X. Y.; Wang, Q. S.; Huang, Y. et al. Enhanced electrochemical H_2 evolution by few-layered metallic $WS_{2(1-x)}Se_{2x}$ nanoribbons. *Adv. Funct. Mater.* **2015**, *25*, 6077–6083.

[44] Ressler, T. *WinXAS*: A program for X-ray absorption spectroscopy data analysis under MS-windows. *J. Synchrotron Rad.* **1998**, *5*, 118–122.

[45] Ankudinov, A. L.; Ravel, B.; Rehr, J. J.; Conradson, S. D. Real-space multiple-scattering calculation and interpretation of X-ray absorption near-edge structure. *Phys. Rev. B* **1998**, *58*, 7565–7576.

[46] Kresse, G.; Furthmiiller, J. Efficiency of *ab-initio* total energy calculations for metals and semiconductors using a plane-wave basis set. *Comput. Mater. Sci.* **1996**, *6*, 15–50.

[47] Mortensen; J. J.; Hansen, L. B.; Jacobsen, K. W. Real-space grid implementation of the projector augmented wave method. *Phys. Rev. B* **2005**, *71*, 035109.

[48] Perdew, J. P.; Burke, K.; Ernzerhof, M. Generalized gradient approximation made simple. *Phys. Rev. Lett.* **1996**, *77*, 3865–3868.

[49] Monkhorst, H. J.; Pack, J. D. Special points for Brillouin-zone integrations. *Phys. Rev. B* **1976**, *13*, 5188–5192.

[50] Fan, X. L.; Wang, S. Y.; An, Y. R.; Lau, W. Catalytic activity of MS_2 monolayer for electrochemical hydrogen evolution. *J. Phys. Chem. C* **2016**, *120*, 1623–1632.

[51] Chou, S. S.; Sai, N.; Lu, P.; Coker, E. N.; Liu, S.; Artyushkova, K.; Luk, T. S.; Kaehr, B.; Brinker, C. J. Understanding catalysis in a multiphasic two-dimensional transition metal dichalcogenide. *Nat. Commun.* **2015**, *6*, 8311.

[52] Nørskov, J. K.; Bligaard, T.; Logadottir, A.; Kitchin, J. R.; Chen, J. G.; Pandelov, S.; Stimming, U. Trends in the exchange current for hydrogen evolution. *J. Electrochem. Soc.* **2005**, *152*, J23–J26.

[53] Faber, M. S.; Dziedzic, R.; Lukowski, M. A.; Kaiser, N. S.; Ding, Q.; Jin, S. High-performance electrocatalysis using metallic cobalt pyrite (CoS_2) micro- and nanostructures. *J. Am. Chem. Soc.* **2014**, *136*, 10053–10061.